

Crown ether decorated silicon photonics for safeguarding against lead poisoning

Received: 24 October 2023

Accepted: 14 April 2024

Published online: 14 May 2024

 Check for updates

Luigi Ranno ^{1,7}, Yong Zen Tan^{2,7}, Chi Siang Ong², Xin Guo³, Khong Nee Koo⁴, Xiang Li³, Wanjun Wang³, Samuel Serna¹, Chongyang Liu⁵, Rusli³, Callum G. Littlejohns⁶, Graham T. Reed ⁶, Juejun Hu ¹, Hong Wang ³ & Jia Xu Brian Sia ^{1,3} ✉

Lead (Pb²⁺) toxification is a concerning, unaddressed global public health crisis that leads to 1 million deaths annually. Yet, public policies to address this issue have fallen short. This work harnesses the unique abilities of crown ethers, which selectively bind to specific ions. This study demonstrates the synergistic integration of highly-scalable silicon photonics, with crown ether amine conjugation via Fischer esterification in an environmentally-friendly fashion. This realizes an integrated photonic platform that enables the *in-operando*, highly-selective and quantitative detection of various ions. The development dispels the existing notion that Fischer esterification is restricted to organic compounds, facilitating the subsequent amine conjugation for various crown ethers. The presented platform is specifically engineered for selective Pb²⁺ detection, demonstrating a large dynamic detection range, and applicability to field samples. The compatibility of this platform with cost-effective manufacturing indicates the potential for pervasive implementation of the integrated photonic sensor technology to safeguard against societal Pb²⁺ poisoning.

Anthropogenic lead (Pb²⁺) poisoning represents one of the primary public health concerns since antiquity. Pb²⁺ is a cumulative toxicant that leads to multifaceted impact on biological functions^{1–5}. Pb²⁺ has the affinity to substitute other bivalent and monovalent cations. For instance, Pb²⁺ can replace Ca²⁺ ions to cross the blood-brain barrier, resulting in neurological deficits¹. This effect is exacerbated in children due to the ongoing development of their neurological and nervous system². Pb²⁺ is also found to impact cardiac function, causing a reduction in the speed of heart contraction and relaxation⁴. Furthermore, fetal exposure can result in a wide array of risks during pregnancy³. The above examples only serve to highlight a non-exhaustive overview of the impact of Pb²⁺ on our society⁶. However,

public actions against lead toxification are disproportional to its impact. It has been estimated that lead service lines still deliver drinking water to about ten million households in the United States⁷. The impact of Pb²⁺ leads to the conclusion that there should be zero tolerance to lead exposure. To that effect, the Environmental Protection Agency (EPA), US has implemented a limit of 15 parts-per-billion (ppb) in drinking water⁸. Lead poisoning is even more pronounced in developing countries, where the World Health Organization (WHO) estimates that of the 240 million people that are overexposed, 99% comes from developing countries^{9,10}. Pb²⁺ exposure accounts for more than one million deaths annually, with significant societal and economic costs, specifically in developing countries^{9,10}. These facts

¹Department of Materials Science & Engineering, Massachusetts Institute of Technology, Cambridge, MA, USA. ²Fingate Technologies Pte Ltd, 8 Cleantech Loop #06-65, 637145 Singapore, Singapore. ³School of Electrical and Electronic Engineering, Nanyang Technological University, 50 Nanyang Avenue, 639798 Singapore, Singapore. ⁴Vulcan Photonics SDN. BHD. D-11-08, Menara Suezcap 1 KL Gateway, No. 2, Jalan Kerinchi, Kampung Kerinchi, 59200 Kuala Lumpur, Malaysia. ⁵Temasek Laboratories, Nanyang Technological University, 50 Nanyang Avenue, 637553 Singapore, Singapore. ⁶Optoelectronics Research Centre, University of Southampton, Southampton SO17 1BJ, UK. ⁷These authors contributed equally: Luigi Ranno, Yong Zen Tan.

✉ e-mail: jiaxbrian.sia@ntu.edu.sg

highlight the urgency for the development of technologies that guard against Pb^{2+} toxicification.

Contemporary methods for Pb^{2+} detection can be grouped into two primary categories: Inductively Coupled Plasma Mass Spectrometry/Optical Emission Spectroscopy (ICP-MS/OES)¹¹, and colorimetric test strips¹². The former represents the state-of-art, but however, suffers from low sample throughput, requiring extensive sample preparation. Furthermore, such systems are dedicated for lab use only, and not viable for *in-operando* analysis¹¹. Colorimetric strips, while low-cost, are qualitative and might lack accuracy¹². The crown ether-decorated silicon photonic (SiP) sensing platform realizes chip-scale integration of these sensor systems. This enables highly quantitative and selective sensing as well as rapid, portable detection capabilities within a fully integrated platform. It is noted that predating the demonstration of this work, there have been significant development in discrete sensors based on square wave anodic stripping voltammetry (SWASV) electrochemistry^{13,14}, fluorescence¹⁵, colorimetry (quantitative)¹⁶, and more lately, fiber-based technologies¹¹ with impressive performances. However, discrete sensors require analytical instruments on a separate platform, limiting the scalability of implementation. This is distinct from our photonic platform in view of its compatibility with waveguide-based analytical components¹⁷ within the SiP ecosystem. Supplementary Note 1 provide an overview and discussion of our platform and the abovementioned technologies.

The photonic sensor platform in this work makes use of crown ethers, cyclic polyethers consisting of multiple oxygen atoms, forming a ring structure¹⁸. These class of compounds were first synthesized by Charles Pederson in the 1960s, who was subsequently awarded the 1967 Nobel prize for this discovery¹⁹. As a result of the cavity, which arises from the ring structure, crown ethers possess a remarkable ability to selectively bind to certain ions or molecules based on their properties such as size selectivity, charge accommodation, ring geometry, and structure energetic favorability^{19–21}. Crown ethers have been demonstrated on electrochemical²² and fluorescence²³-based detection schemes as well. However, as previously outlined, scaling these discrete technologies to low-cost large sensor arrays for widespread detection remains a challenge.

In this manuscript, we demonstrate a crown ether functionalized SiP platform. Traditionally, the functionalization of crown ether on silicon involves the use of silylating agents with trisubstituted silyl groups, which are moisture and pH-sensitive, and require stringent process control^{24,25}. In the above protocol, the reagents can potentially undergo self-reaction, resulting in agglomeration, which decreases surface uniformity, impacting sensor reproducibility^{24,25}. The application of the Fischer esterification protocol²⁶ to couple carboxylic acid groups with the -OH group on pretreated SiO_2 waveguides surfaces, demonstrated in this study, can circumvent the aforementioned problem and produce the uniform amine conjugation of crown ethers on the SiO_2 -coated waveguide surfaces (see below Fig. 3a). We note that the successful Fischer esterification on SiO_2 defies the conventional view that the reaction is applicable to organics only²⁶. Toward a broader scope, the Fischer esterification of an inorganic material possessing an -OH group implies the surface-agnostic nature of this process (-OH group), indicating far-reaching technological implications to replace silylation agents in cases where they are used to couple silica/silicon with organic compounds^{24,25}. For instance, different crown ethers^{27–37}, selective to various ions (i.e., K^{30} , Be^{31} , Ra^{33} , Cs^{28}), illustrated at the inset of Fig. 1e, can undergo amine conjugation following Fischer esterification on SiO_2 , greatly broadening the range of applications (i.e., medical³⁰, electronics manufacturing³¹, nuclear^{28,33}) that the developed platform can be extended to. As a corollary of complementary metal-oxide-semiconductor (CMOS) fabrication, SiP has proven to be a disruptive integrated photonic technology that enables high-precision mass manufacturing³⁸. Through the synergistic integration of both technologies, the resulting platform is engineered to

overcome several unaddressed issues against lead poisoning in society: 1). The successful amine conjugation of crown ethers via Fischer esterification onto aptly designed SiP circuits will enable the selective, ppb-scale detection of Pb^{2+} ions with large dynamic range (1–62000 ppb), improving upon current bulky lab-based systems (ICP-MS/OES)¹¹ in terms of portability. The photonic sensor enables the detection of Pb^{2+} concentrations below the EPA limit (15 ppb)⁸. Moreover, the large upper bound of detection broadens its applicability to heavy industries such as mining³⁹, smelting⁴⁰, battery manufacturing⁴⁰, effluent monitoring⁴⁰ where detection at the tens of part-per-millions (ppm) is mandated. 2.) ICP-MS/OES requires a significant lead time from sample collection to results due to complex lab-based sample processing and analysis¹¹. Our sensor enables a single measurement to be performed in ~120 s. This is in addition to its ability to maintain high detection accuracies across a pH range of 6–8 (limited by Pb solubility at higher pH⁴¹), encompassing typical environmental conditions⁴², without requirements on sample processing. This indicates the capacity for rapid, *in operando* determination of Pb^{2+} concentration on site. 3). The viability of the sensor platform is assessed using field-collected samples (including tap, lake and seawater samples), where no impairment in detection accuracies was observed. This highlights the potential of the sensor to be applied in real life applications. 4). The high-index contrast of silicon against its cladding material (SiO_2) enables the design of compact integrated photonic sensors. The realization of the Pb^{2+} -selective sensor within the SiP ecosystem implies compatibility with established waveguide-based analytical components (i.e., spectrometer¹⁷). This enables sensor system integration (sensor and analytics¹⁷) at the chip-scale. 5). Through established silicon manufacturing, SiP circuits can be mass-produced at low cost³⁸. Furthermore, the crown-ether functionalization process is solution-based (reactants dissolved in green solvents, such as water and ethanol), implying that wafer-scale functionalization can be achieved, indicating scalability, with minimal environmental pollution. The ability of the integrated platform to leverage on highly-precise, scalable, and cost-effective fabrication techniques serves to decrease the price of compact and portable Pb^{2+} sensor systems, without compromising performance. This encourages the much-needed proliferation of such Pb^{2+} detection systems in society.

Concept

Photonic device design

The Pb^{2+} sensor illustrated in Fig. 1a, is fabricated on the 220 nm silicon-on-insulator platform; the silicon device layer is 220 nm thick. As indicated in Fig. 1b, the sensor consists of 3 primary technology sub-layers: SiP, Fischer esterification, and crown ether-based functionalized layer. Fischer esterification lays the ground for the amine conjugation of crown ethers, where the subsequent change in the material index of the crown ether-based functional layer upon detection of Pb^{2+} ions is translated into the optical domain via SiP. The micrograph image of the sensor is shown in Fig. 1c. Slot waveguides are implemented in the sensing region (H_2O cladding in the aqueous phase). As the slot width is comparable to the exponential decay length of the fundamental eigenmode, optical power perpendicular to the high-index contrast interfaces is amplified^{43,44}. Essentially, this feature of slot waveguides lends to high surface sensitivity^{43,44}. The input light-wave propagates to an asymmetric adiabatic tapered splitter⁴⁵ (Fig. 2d), where a larger proportion of the optical power is directed to the sensing path. Following, a 250 μm -long strip-to-slot converter is utilized for the transition of the strip-to-slot optical mode⁴⁶ (Fig. 2e). With the exception of the sensing region (Fig. 1a, b), which is exposed to the analyte in the aqueous phase, the entire device is cladded with SiO_2 . The thickness of the SiO_2 cladding is designated to be 2 μm to prevent interaction with the analyte, where >99% of the optical power is confined within the cladding. In the reference arm, slot waveguides with identical dimensions are also implemented. This is to normalize

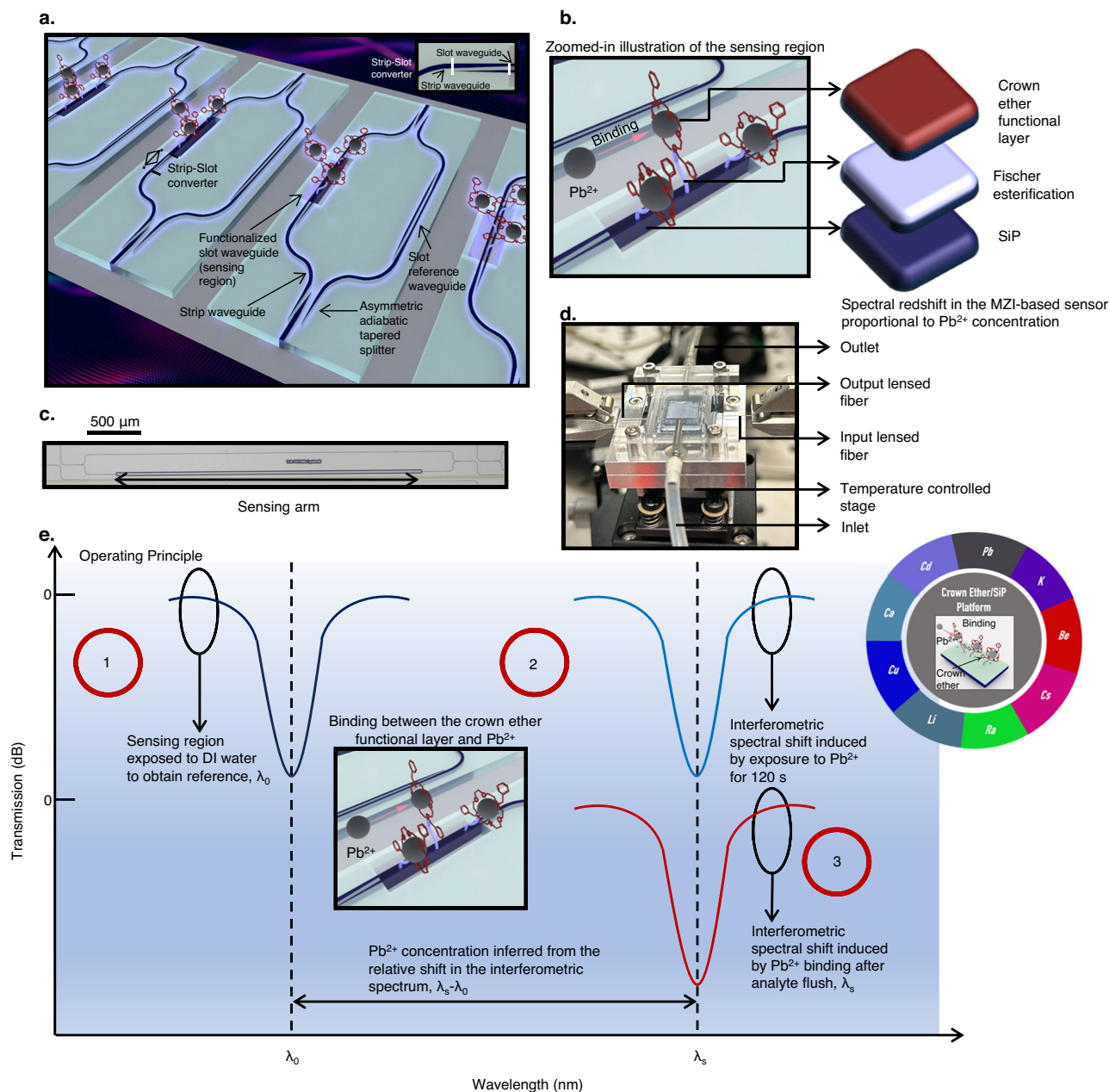


Fig. 1 | Concept of the Crown Ether/SiP platform for Pb^{2+} ion detection. **a** 3-D illustration of the photonic Pb^{2+} ion sensor based on the crown ether-decorated SiP platform. The functionalization performed in the sensing region is indicated. For the sake of clarity, the 20 nm SiO_2 deposited on top of the waveguides in the sensing region is not indicated. Information is provided in Fig. 3a. **b** The zoomed-in illustration of the sensing region, where the binding between the Pb^{2+} ions and crown ether functional layer is depicted. The technology sub-layers in the sensing

region are labeled: SiP, Fischer esterification, and the crown ether functional layer. **c** Micrograph image of the Pb^{2+} ion sensor, where the sensing arm and scale bar (500 μm) are indicated. **d** The Pb^{2+} photonic sensor assembly, consisting of the photonic chip and a microfluidic chamber. **e** Elucidated operating principle of the photonic Pb^{2+} ion sensor. The inset shows the exemplary applications that the ion detection platform can be extended to.

waveguide propagation losses on the sensing and reference arms, and the power ratio of the asymmetrical adiabatic tapered splitters are designed according to H_2O absorption⁴⁷ (designed losses) in the sensing region. The lightwave from the sensing and reference arms recombines at the asymmetrical adiabatic tapered splitter, forming the MZI interferometric spectrum. The power ratio of the two splitters is designed to optimize interference fringe visibility⁴⁸ (extinction ratio). The operating protocol of the sensor is elucidated in Fig. 1e. First of all, the sensing arm is exposed to deionized (DI) water to obtain the reference resonant wavelength (λ_0); subsequent wavelength shift is considered in reference to this wavelength.

Then, DI water is flushed from the microfluidic chamber, and an analyte possibly containing Pb^{2+} ions is added and exposed for 120 s. The temporal dependence of the sensor is analyzed through the crown ether functional layer via X-ray Photoelectron Spectroscopy (XPS) where the signal strength rises from 10 s to 120 s and remains stable after (See Supplementary Note 2). To that effect, all the following analyte exposure times are standardized at 120 s. Should the analyte contain Pb^{2+} , a resonant shift is induced through the binding of ions to the functionalized surface of the sensing region via surface sensing⁴⁴. However, one should also note that a proportion of the wavelength shift could also be caused by the interaction of the evanescent field

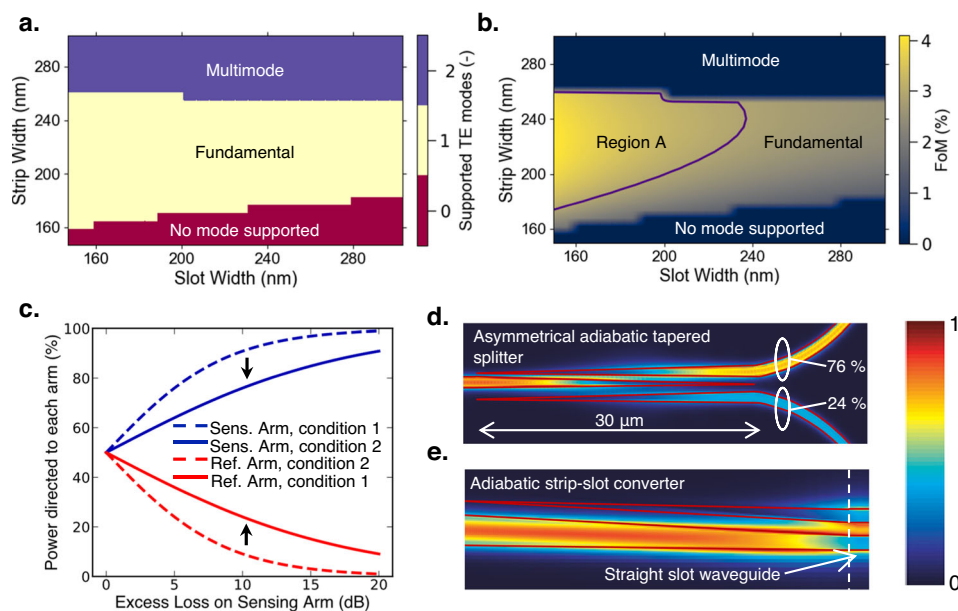


Fig. 2 | Photonic design of the Pb^{2+} ion sensor. **a** Simulation of the number of supported TE optical modes in the slot waveguides as a function of strip and slot width. **b** Sensor surface sensing FoM as a function of strip and slot width. **c** The comparison of two proposed splitting Mach-Zehnder architectures (see Supplementary Note 5) in terms of the power asymmetry required of the splitter;

condition 1 ($S_1 = S_2, S'_1 = S'_2, S'_{1/2} \neq 0.5$), condition 2 ($S'_1 \neq 0.5, S'_2 = 0.5$). Top-down electric field distribution of the **d**, asymmetrical adiabatic tapered splitter, and **e**, adiabatic strip-slot converter, where the structures of the components are outlined.

with the other particles/ions/molecules in the analyte⁴⁴. Therefore, this necessitates the subsequent flushing of the analyte from the device via DI water. This results in the retention of Pb^{2+} ions, which are bound to the surface of the sensing region through the crown ether-based functionalized layer, where Fig. 1b provides a further illustration. The complexation of Pb^{2+} ions with the crown ether can be understood through the interaction of the 6s2 electrons and accepting 6p orbitals with the electron lone pairs on the donating oxygen and nitrogen groups on the crown^{49,50}. When Pb^{2+} ions are bound to the crown ether-based functional layer, the high electron density of Pb^{2+} increases the polarizability of the functional layer^{51,52}. This results in a rise in the relative permittivity of the functional layer. Consequently, the material refractive index increases with higher relative permittivity. Subsequently, due to the higher group index of the sensing waveguide as compared to the reference arm, an increase in the material index of the functional layer will lead to a resonant redshift ($\lambda_s - \lambda_0$), attributed to the crown ether-immobilized Pb^{2+} ions in the sensing region. The concentration of the Pb^{2+} ions in the analyte can then be deduced from the relative shift in resonance wavelength from reference ($\lambda_s - \lambda_0$), utilizing a calibration curve; the calibration curve indicates ($\lambda_s - \lambda_0$) as a function of Pb^{2+} concentration (see below Fig. 5b). We will henceforth refer to the flushing of analyte and the addition of DI water into the microfluidic chamber after ion interaction as analyte flush.

Figure 1d shows the photonic chip, with the polydimethylsiloxane (PDMS) microfluidic channel mounted via a stainless-steel fixture. The microfluidic channel is designed to hold 0.426 ml of analyte, where the solution is filtered through a syringe filter (0.45 μm) prior to sensor exposure. Analyte input and extraction was implemented via the following inlet and outlet tubes. Optical input/output was performed via edge coupling between a lensed fiber with $\sim 3 \mu\text{m}$ mode field diameter and a silicon coupler that tapers down to 175 nm wide. The above-mentioned assembly (see Supplementary Note 3) was mounted on top of a thermoelectric controller (TEC), maintained at 296 K with a thermal drift of lower than 2 mK.

The dimensions of the slot waveguide (Supplementary Note 4) were determined via eigenmode calculations in Fig. 2a, b, where H_2O

cladding surrounds the structure. The parameter space corresponding to the number of transverse electric (TE) modes was performed in Fig. 2a. As the top and bottom media surrounding the waveguide are asymmetrical (BOX on the bottom and H_2O as the cladding), there exists a regime where the fundamental mode is not supported (in red). Conversely, the multi-mode regime of the slot waveguide structure is indicated in blue, where the second-order TE mode can be supported. According to Fig. 2a from left to right, the second-order TE mode emerges when the strip and slot widths are ~ 260 and ~ 145 nm, respectively. In addition, the corresponding strip width that excites the second-order TE mode decreases as slot width increases. The parameter space corresponding to single TE mode propagation is highlighted in yellow. For optimization of surface sensitivity, the selection of the optimal strip and slot width, subject to the fundamental TE mode, is dependent on the optical mode confinement on the surface of the sensing region. To that effect, a figure-of-merit (FoM) is defined, that takes into consideration the optical confinement factor within 10 nm about the surface of the slot waveguides, which are cladded with 20 nm of SiO_2 (see Supplementary Note 4).

Computation of the FoM is performed in the parameter space of Fig. 2a and the results are presented in Fig. 2b. The corresponding boundary condition for the number of supported TE modes (Fig. 2a) is replicated in Fig. 2b. As a guide to the eye, the highest value of FoM is indicated by region A. However, we have encountered difficulties in the selective removal of SiO_2 cladding at the sensing region when the slot gap is smaller than 200 nm. As such, strip and slot width of 240 and 240 nm, respectively are implemented to relax process requirements; the selected slot waveguide parameters lie close to the boundary of region A.

H_2O poses significant water absorption at the C-band⁴⁷. Yet, the length of the sensing region increases the surface sensitivity; which forces an inherent tradeoff between the fringe visibility (extinction ratio) and sensitivity⁴⁴. The implementation of asymmetrical splitting in MZIs will serve to overcome the issue. As identical slot waveguide dimensions are implemented on the sensing and reference arms, the primary source of loss difference between the two arms comes from

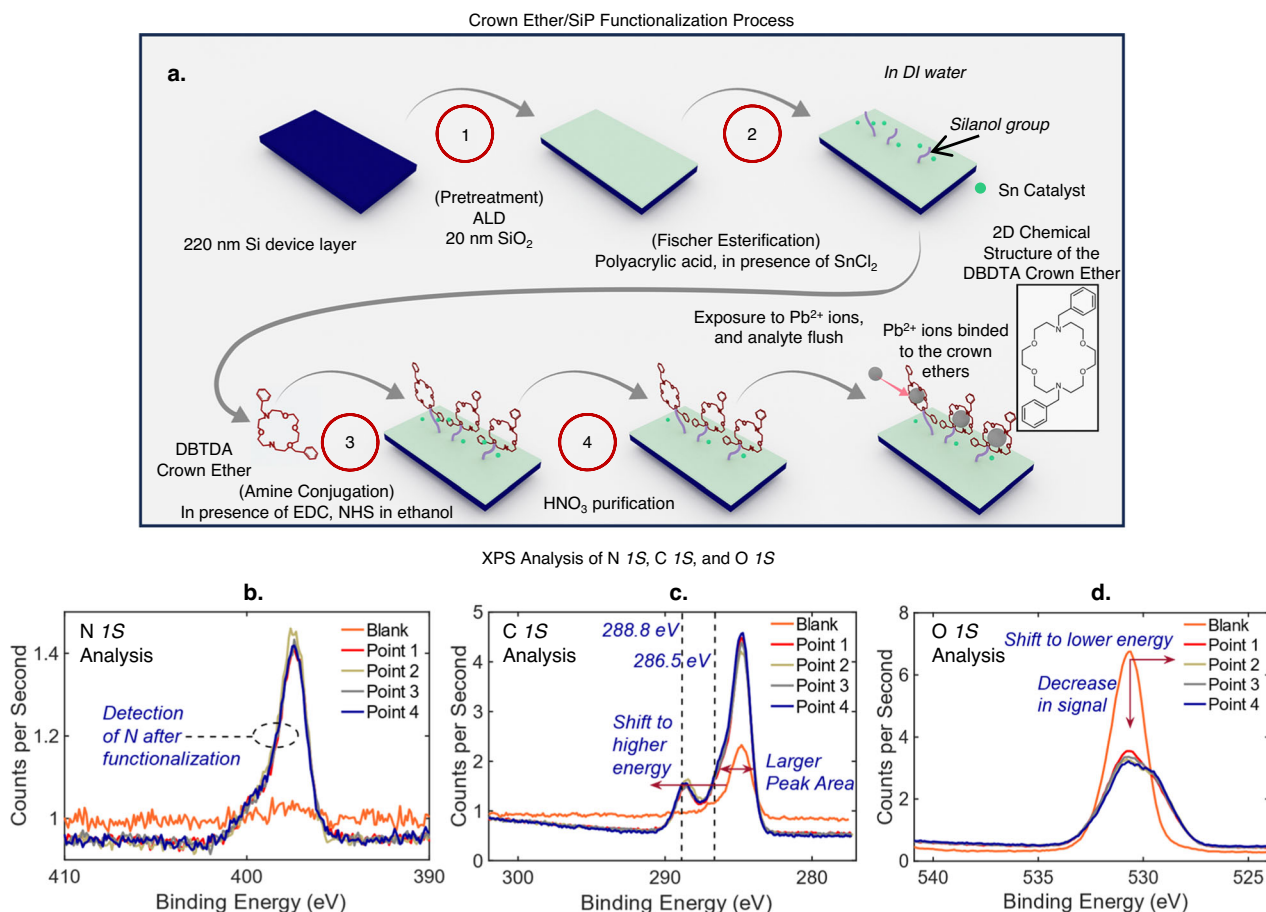


Fig. 3 | The development of the Crown Ether/SiP functionalization process. **a** The developed crown ether/SiP functionalization process, described in four steps; the 2D chemical structure of the DBTDA crown ether is illustrated. XPS

narrow spectra analysis of the **b**, N 1S, **c**, C 1S, **d**, O 1S regions of the photonic chips, before and after functionalization.

water absorption. It can be concluded that the splitting ratios of the MZIs must be co-designed with the length of the sensing arm, hence designed losses. The quantities are related to one another via the following equation, where the derivation is elaborated (see Supplementary Note 5). Designed losses through water absorption is assumed to be the only source of loss in the sensor.

$$\sqrt{S_1} \sqrt{S_2} e^{-\frac{\alpha L}{2}} = \sqrt{S'_1} \sqrt{S'_2} \quad (1)$$

S_1, S'_1 and S_2, S'_2 refers to the splitting ratios of the input and output splitters, respectively. Assuming the splitters are lossless, energy conservation dictates that $S_{1/2} = 1 - S'_{1/2}$. α is the loss coefficient due to water absorption, and L refers to the length of the sensing arm. We propose a condition such that $S_1 = S_2$, $S'_1 = S'_2$ and $S'_{1/2} \neq 0.5$ (condition 1). In Fig. 2c, we plot the splitting ratios to the sensing and reference arm corresponding to maximum visibility. A comparison to an alternate condition where arbitrary splitting is at the input splitter, and 3-dB splitting is at the output splitter (condition 2, $S'_1 \neq 0.5, S'_2 = 0.5$) is also indicated in Fig. 2c; see Supplementary Note 5. In comparison, condition 1 reduces the asymmetry that is required of the splitters, alleviating fabrication requirements. As a compromise between the sensor surface sensitivity and the optical measurement setup power budget, our demonstration selected splitting ratios corresponding to sensor arm designed loss of 10 dB: $S_1 = 0.76, S_2 = 0.24$. In regard to the selected slot waveguide dimensions in a water cladding, the waveguide propagation loss due to H₂O absorption is estimated to be 35 dB/cm at

$\lambda = 1.55 \mu\text{m}$. This gives rise to a sensing arm length of $\frac{\text{Designed Loss (dB)}}{\text{Propagation Loss (dB/cm)}} = \frac{10}{35} = 2857.14 \mu\text{m}$.

Asymmetrical adiabatic tapered splitter, which has been developed in our previous work⁴⁵, are implemented for arbitrary power splitting. In Fig. 2d, we show the top-down electrical field distribution of a 30 μm -long 76/24% power splitter. The length of the strip-to-slot converter is 250 μm , where low-loss adiabatic conversion from strip to slot mode is facilitated⁴⁶. Similarly, the top-down electric field distribution of the lightwave as it propagates along the converter is indicated in Fig. 2e.

Functionalization and characterization of 7,16-dibenzyl-1,4,10,13-tetraoxa-7,16-diazacyclooctadecane (DBTDA) crown ether functionalized chip via Fischer esterification and amine conjugation

The functionalization protocol can be divided into four steps (Fig. 3a) with cleaning of excess reactants implemented after every step. Firstly, a layer of SiO₂ (20 nm) is deposited onto silicon via Atomic Layer Deposition (ALD) in the pretreatment step. Secondly, the Fischer esterification method²⁶ is used to couple the silanol group on the SiO₂ surface of the SiP slot waveguides (in the sensing region) with polyacrylic acid ((C₃H₄O₂)_n), in the presence of a tin catalyst⁵³; specifically tin (II) chloride (SnCl₂) dissolved in DI water. The photonic chips, immersed in the reagent, was maintained at 318 K and agitated, while the reaction proceeds for 60 minutes. The chips are then cleaned with DI water. Following, the photonic chips are functionalized with the DBTDA crown ether, forming amide bonds via conjugation, in the

presence of 1-Ethyl-3-(3-dimethylaminopropyl)-carbodiimide (EDC) and N-Hydroxysuccinimide (NHS) dissolved in ethanol^{11,54}. In the final step, the functionalized photonic chips are rinsed in dilute nitric acid (HNO₃) to remove as much of tin catalyst adsorbed on the surface as possible. This was done by placing the functionalized photonic chips in a solution of 0.1M HNO₃, agitated with a magnetic stir bar for 60 minutes. Details pertaining to the chemicals used for functionalization is elucidated in the Methods section.

XPS analysis was used to characterize the functionalized photonic chips before functionalization, as well as before and after interaction with different ions to analyze the resulting elemental constitution. A comparison of the *N 1s* region⁵⁵ of the XPS spectrums before and after functionalization (Fig. 3b) shows that the presence of nitrogen is only detected after the functionalization process. Furthermore, a comparison of the *C 1s* region⁵⁵ of the XPS spectrums before and after functionalization (Fig. 3c) shows a larger peak area and chemical shift of *C 1s* carbon towards higher binding energies (-286.5 eV⁵⁵, -288.8 eV⁵⁵) following functionalization. The binding energy level at 286.5 eV indicates higher carbon concentration and significant carbon binding with electronegative species such as oxygen (C-O) and nitrogen (C-N)⁵⁵, and the peak at -288.8 eV corresponds to C=O⁵⁵. Furthermore, the comparison of the *O 1s* region⁵⁵ of the XPS spectrums before and after functionalization (Fig. 3d) shows a decrease in oxygen signal and chemical shift of *O 1s* towards a lower binding energy.

This observation can be attributed to the functional layer consisting of more carbon compared to oxygen⁵⁵, and the Fischer esterification of silanol with the carboxylic acid group forms O-C bonds, which have a lower binding energy compared to O-Si bonds⁵⁵. The above shows significant evidence that Fischer esterification have been successfully achieved following the elucidated protocol (Fig. 3a). To assess the uniformity of functionalization, in Fig. 3b–d, the *N 1s*, *C 1s* and *O 1s* regions respectively of the XPS spectra were taken at four different points (Point 1, 2, 3, 4) on the photonic chip spaced more than 1 cm apart on the photonic chip, showing high consistency. This implies that a functional layer with good uniformity have been realized. In addition, Energy Dispersive X-ray (EDX) analysis pertaining to the functional layer was performed and included in Supplementary Note 6. The results provide compelling evidence for the uniform functionalization of the DBTDA crown ether, which contains carbon bonded to nitrogen and oxygen, via Fischer esterification and amine conjugation.

Na⁺, K⁺, Mg⁺, Li⁺, Zn²⁺, Ca²⁺, Fe²⁺, Cu²⁺, Al³⁺, Sn²⁺, Cd²⁺, and Pb²⁺ were chosen as highly relevant analytes to quantify the selectivity of the photonic-based detection platform. The selected ions possess a variety of ionic sizes and charge. Na⁺, K⁺, Ca²⁺, Mg⁺, Zn²⁺ and Cu²⁺ are commonly found in bottled water sources⁵⁶, while Fe²⁺, Li⁺, and Al³⁺ could be present in groundwater sources⁵⁷. Sn²⁺ is used as a catalyst in the Fischer esterification process⁵³, and Cd²⁺ and Pb²⁺ are toxic heavy metals that should be prohibited in drinking water⁵⁸. Each functionalized photonic chip interacts with of the abovementioned ions (DI water, pH = 6.8) independently for 120 s in a microfluidic chamber; see Methods for analyte preparation. After which, the analyte is flushed with DI water and dried with N₂ gas blow. XPS is utilized to identify the elemental constitution on the surface of the photonic chips before and after ion interaction via the respective elemental binding energies of each element. Normalization was carried out where the narrow scan XPS spectra prior to ion interaction was subtracted from that after ion interaction. The normalized narrow scan XPS spectra of Na⁺, K⁺, Mg⁺, Li⁺, Zn²⁺, Ca²⁺, Fe²⁺, Cu²⁺, Al³⁺, Sn²⁺, and Cd²⁺ are displayed in Fig. 4a–k, respectively, indicating the absence of binding on the functionalized photonic sensor. For the abovementioned ions, we note that only Sn²⁺, which is used as the catalyst during Fischer esterification, have been identified prior to ion interaction (see Supplementary Note 7). Conventionally, Fischer esterification is favored when H₂O is removed as the reaction proceeds (dehydrative esterification). However, the

developed esterification process in this work utilizes H₂O as a green solvent, which will decrease the catalytic activity of Brønsted acid catalysts (i.e., H₂SO₄)⁵⁹. To that effect (Fig. 3a), the H₂O-tolerant Lewis acid catalyst SnCl₂, is used^{53,60} where Sn is embedded into the SiO₂, functioning as a heterogeneous catalyst in the process. It is known that heterogeneous catalysts show improved catalytic activity⁶¹ that favors esterification even in the presence of H₂O⁶². This is verified in Fig. 3b–d and Supplementary Note 6, 7. In Fig. 4i, unmistakable binding of Pb²⁺ ions are demonstrated, indicating the presence of Pb²⁺ binding events on the functional layer, via identification of the Pb *4f*_{5/2} and Pb *4f*_{7/2} elemental binding energies⁵⁵. Furthermore, in Supplementary Note 6, EDX analysis is performed, where the absence and presence of Pb²⁺ can be clearly seen before and after interaction respectively. From the above, it can be anticipated that the photonic sensor will be selective only towards Pb²⁺, where the ion will bind to the functionalized surface, and be present after analyte flushing. Subsequently, the concentration of exposed Pb²⁺ can be inferred from photonic surface sensing via the shift ($\lambda_s - \lambda_0$) in the interferometric spectrum.

Pb²⁺ photonic sensor characterization

In Fig. 5a, we show the measured fundamental TE mode transmission of the photonic sensor, exposed to DI water (pH = 6.8); see Methods for maintenance of fundamental TE. Details of SiP chip fabrication is elaborated in Supplementary Note 8. As predicted, good interference fringe visibility is obtained, at $\lambda = 1531.9$ nm, where extinction ratio exceeds 20 dB. In contrast, when the sensing region is exposed to air, poor visibility is observed (see Supplementary Note 9). The sensor visibility is reduced at $\lambda = 1563.7$ nm, attributed by the lower water absorption at $\lambda = 1563.7$ nm. The experimental demonstration of the sensor visibility is limited by fabrication bias from design parameters. This would induce changes in designed splitting ratios (S_1, S'_1, S_2, S'_2), as well as loss difference between the reference and sensing arms. The measured free-spectral range (FSR) is 31.7 nm.

The calibration curve of the Pb²⁺ sensor, indicating ($\lambda_s - \lambda_0$) as a function of cumulative Pb²⁺ concentration within the analyte (5, 25, 125, 625, 2625, 12,625, 62,625, 262,625 ppb) is indicated in Fig. 5b through a cumulative testing process (see Methods) with the associated error bars, obtained via six independent measurements ($n = 6$); the inset shows ($\lambda_s - \lambda_0$) within a range of 1 to 10 ppb. The pH of the analyte utilized in Fig. 5 is maintained at 6.8 in DI water. A fit was performed between the measured values to understand the form of the calibration curve. The mathematical relationship between ($\lambda_s - \lambda_0$) and exposed Pb²⁺ reference concentration is indicated in Supplementary Note 10. The sigmoidal curve is characteristic of (i) absorption isotherms^{63,64}, attributed by the binding of Pb²⁺ ions to the crown ether functional layer, and (ii) light-matter interaction between the waveguide mode and the functional layer with Pb²⁺ bonded. In Fig. 5c, we show a set of MZI spectra around the minima transmission points for the fringes corresponding to each of the abovementioned concentrations. As a large cumulative concentration range is presented in Fig. 5c, the spectra when cumulative Pb²⁺ concentration are 0, 5, and 25 ppb are shown (Fig. 5d). Indicated by the shaded region in Fig. 5b, ($\lambda_s - \lambda_0$) exceeds a single FSR when the cumulative concentration of Pb²⁺ is higher than ~4000 ppb. Saturation of ($\lambda_s - \lambda_0$) against cumulative concentration is observed in Fig. 5b. This is ascribed to the saturation of the binding sites within the functional layer^{63,64}. The lower limit and upper limit of detection are 0.882 ppb and 62600 ppb, respectively, as defined in Supplementary Note 11.

To affirm reproducibility of the calibration curve in Fig. 5b, twenty-four photonic sensors were tested independently, six times each ($n = 6$) at reference concentrations of 1, 10, 80 ppb and 62 ppm. In Fig. 5e, an instance of the transmission spectra when the sensing region is exposed to DI water, DI water containing 80 ppb Pb²⁺, as well as after analyte flush of Pb²⁺ are shown. Based on the positions of λ_s in relative to λ_0 , a ($\lambda_s - \lambda_0$) of 2.89 nm is obtained. This shift was observed

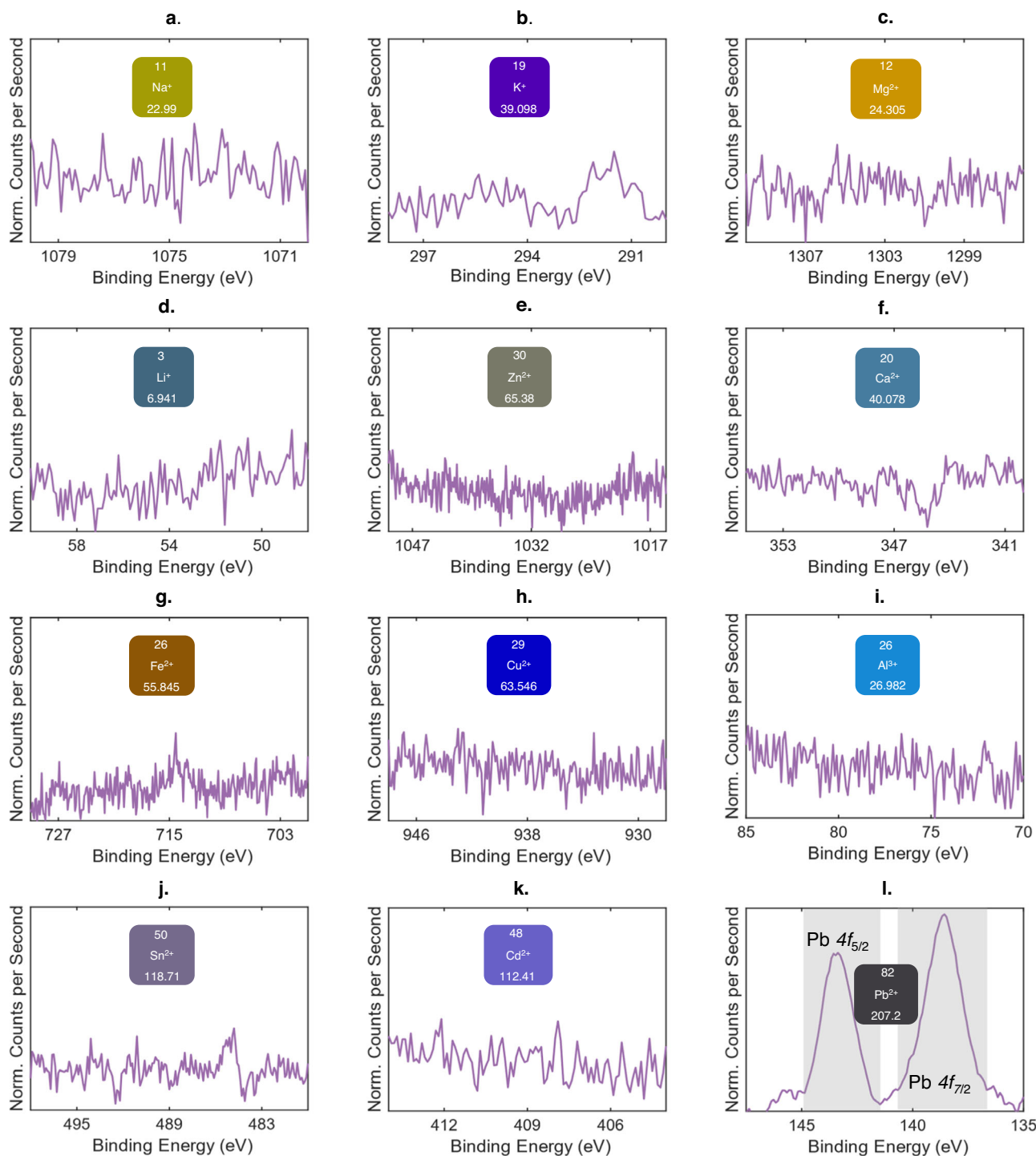


Fig. 4 | Analysis of the crown ether functional layer selectivity via XPS. Normalized narrow scan XPS spectra at the photonic chip surface by subtracting the spectra prior to ion interaction from that of after ion interaction (normalization).

The ions tested are **a**, Na⁺, **b**, K⁺, **c**, Mg²⁺, **d**, Li⁺, **e**, Zn²⁺, **f**, Ca²⁺, **g**, Fe²⁺, **h**, Cu²⁺, **i**, Al³⁺, **j**, Sn²⁺, **k**, Cd²⁺, and **l**, Pb²⁺ at 100 ppb, in DI water. The pH of all the analyte is maintained at 6.8 (see Methods).

after analyte flushing, consistent with the binding mechanism on the surface of the sensor. By comparing this value to Fig. 5b, the inferred concentration from the calibration curve is 81.7 ppb. Repeated measurements ($n = 6$) presented in Table 1 indicate a mean inferred concentration ($\text{Conc}_{\text{mean}}$) of 79.0 ppb with a standard deviation (σ_{conc}) of 1.7 ppb, which is close to the reference value of 80 ppb. The concentration detection error (Err.), defined as the difference in mean sensor inferred concentration from the reference value, is 1.3%. Similarly, Fig. 5f–h shows one of the repeated measurements, performed at

ground truths of 1, 10 ppb and 62 ppm, yielding sensor-inferred concentrations (Fig. 5b) of 1.7, 10.6 ppb and 62.9 ppm, respectively. Likewise, the sensor detection accuracy and repeatability subject to the abovementioned reference standard solutions via multiple measurements ($n = 6$) are presented in Table 1, where $\text{Conc}_{\text{mean}}/\sigma_{\text{conc}}/\text{Err.}$ of 1.24 ppb/0.26 ppb/24%, 10.2 ppb/0.3 ppb/ 2% and 64.6 ppm/4.5 ppm/4.2% are inferred respectively. Due to the large detection dynamic range of the sensor, it is imperative to assess the sensor detection accuracies by absolute detection accuracy near the lower

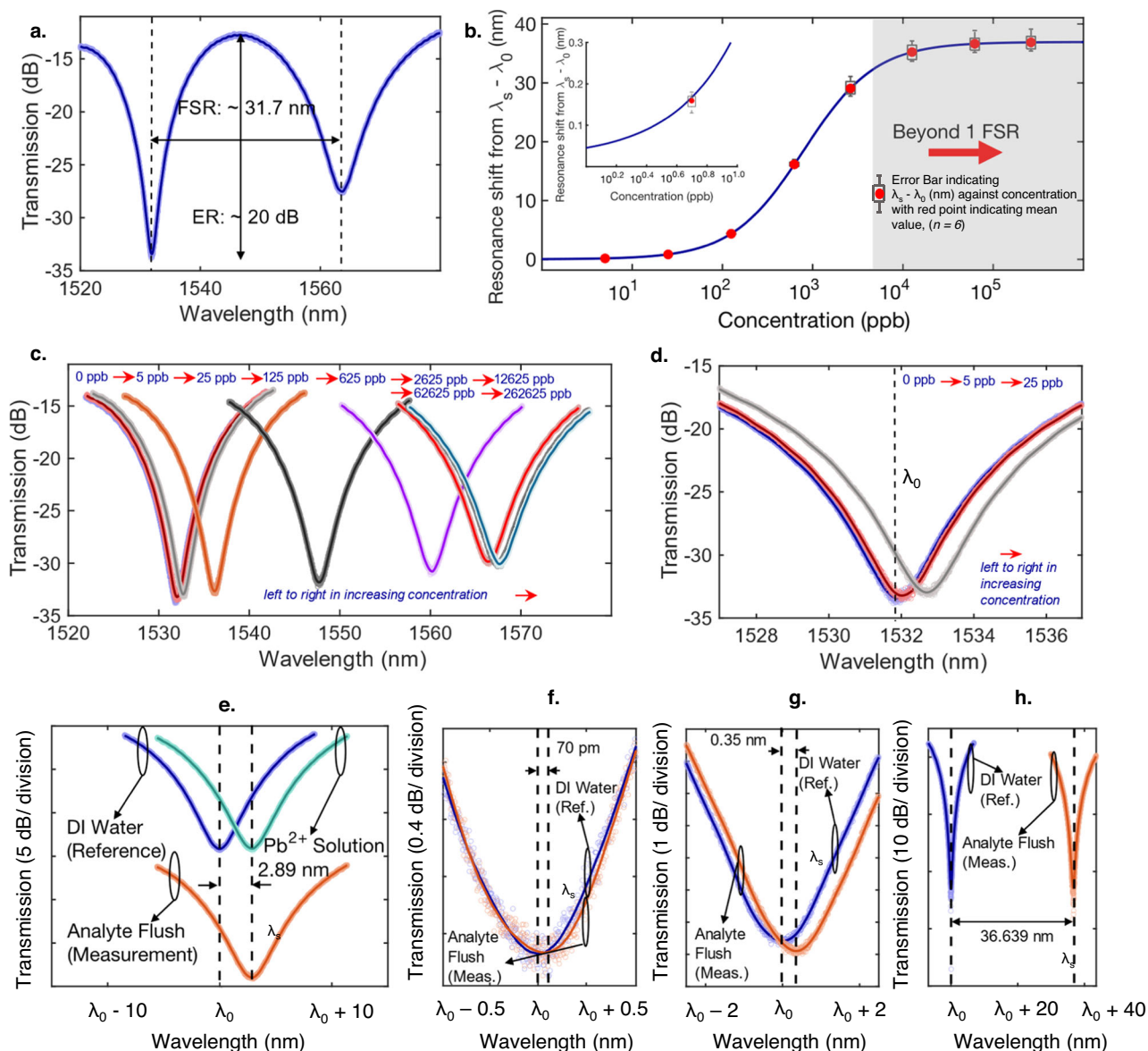


Fig. 5 | Experimental characterization of Pb^{2+} sensor performance. **a** Wavelength spectrum of the sensor, when DI water is applied into the sensor assembly (as shown in Fig. 1d). **b** Calibration curve of the sensor when exposed to reference Pb^{2+} concentration of 0, 5, 25, 125, 625, 2625, 12625, 62625, 262625 ppb via a cumulative testing approach (see Methods). Error bars pertaining to six independent measurements ($n = 6$) are indicated, where the bottom and top edges of the boxplot correspond to the 25th and 75th percentile of the data. The minimum and maximum points of the data are indicated by the extension to which the whiskers of the

boxplot are extended to. The mean of the data is indicated by the red point. **c** A set of optical fringe minima corresponding to the tested concentrations in the calibration curve (Fig. 5b). **d** Fig. 5c, zoomed-in at concentrations of 0, 5, 25 ppb. Validation of the calibration curve (Fig. 5b) at reference concentrations of **e**, 80 ppb, **f**, 1 ppb and **g**, 10 ppb, **h**, 62 ppm. For the detection of Pb^{2+} concentration via the sensor in Fig. b–h, the pH of the analyte is maintained at 6.8 (see Methods). DI water is used.

detection limit, and fractional detection limit approaching the upper detection limit. The large detection dynamic range of the sensor (Figs. 5b, e–h, Table 1), implies broad applicability within the Pb^{2+} sensing application space: from monitoring of drinking water (<15 ppb⁸) to heavy industrial applications such as mining³⁹, smelting⁴⁰, battery manufacturing⁴⁰ and effluent monitoring⁴⁰ where Pb^{2+} concentrations in the tens of ppm is possible. A major benefit of the developed photonic sensors is predicated on its compatibility with scalable and cost-effective processes. This can potentially facilitate the single-use application of the sensors. Alternatively, Supplementary Note 12 also indicates the capacity for reuse.

In Fig. 4 (XPS analysis), the functional layer is found to be selective to Pb^{2+} ions against other tested ions, implying the selectivity of the photonic sensor. To further verify sensor selectivity performance at

the EPA Pb^{2+} safety threshold⁸, Na^+ , K^+ , Mg^{2+} , Li^+ , Zn^{2+} , Ca^{2+} , Fe^{3+} , Cu^{2+} , Al^{3+} , Sn^{2+} , Cd^{2+} are all tested in DI water at reference concentrations of 15 ppb, where the pH of the analyte is maintained at 6.8. The reference interferometric spectrum (in DI water), and the resulting spectrum after exposure and analyte flush for Cd^{2+} and K^+ are presented in Fig. 6a, b respectively. The data for the rest of the ions are presented in Supplementary Note 13. No shifts in the interferometric spectra indicative of ion binding are observed. Similar to Fig. 5e–h, six independent photonic sensors were tested at 15 ppb of Pb^{2+} . In Fig. 6c, an instance of the measured spectra is shown, where a sensor inferred concentration of 15.0 ppb corresponding to 0.504 nm of ($\lambda_s - \lambda_0$) was obtained from Fig. 5b. Repeated measurements ($n = 6$) indicates $\text{Conc.}_{\text{meas}} / \sigma_{\text{conc}} / \text{Err.}$ of 14.3/0.6 ppb/4.7% as summarized in Table 1. The results in Fig. 6 and Supplementary Note 13 underpins the ability

of the sensor to effectively detect Pb^{2+} ions in the presence of the other ions.

Device performance with field samples and speciation of Pb^{2+} ions

The pH tolerance of the Pb^{2+} photonic sensor is of great significance in regard to deployment in practical environmental scenarios. Most environmental water sources where Pb^{2+} are present have a pH range between 6 to 8⁴². It is imperative for the sensor to facilitate accurate and reliable measurements across this pH spectrum. Pb precipitates at higher pH (>9), facilitating the removal of Pb via precipitation⁴¹. While the pH of a sample can be adjusted prior to sensor detection, these processing steps are non-trivial for the untrained personnel and hence can limit the scale of adoption with regards to a sensor technology. In the following section, the pH resilience of the Pb^{2+} photonic sensor technology is evaluated. First of all, the capacity of the crown ether functional layer for Pb^{2+} binding across a pH range of 2–8 in DI water (pH = 6.8) is investigated via XPS. In Fig. 7a, the normalized Pb

$4f_{5/2}$ and $\text{Pb } 4f_{7/2}$ elemental binding energies are shown. It can be seen that the XPS spectra remains similar within a pH range of 6–8. The introduction of H^+ ions within an acidic environment promotes the protonation of oxygen and nitrogen atoms of the crown ether⁶⁵, and a reduction in the electron density of the oxygen and nitrogen atoms results. This decreases the availability of coordination to Pb^{2+} . Moreover, the addition of positive ions will repel the positively charged Pb^{2+} ⁶⁶. The solubility of Pb^{2+} ions decrease significantly at higher pH via precipitation (i.e., $\text{Pb}(\text{OH})_2$)⁴¹ where the accurate aqueous detection of Pb^{2+} becomes solubility-limited. The solubility of Pb^{2+} in water sources is beyond the scope of this study. To that effect, the influence of pH on sensor detection accuracy is assessed at environmentally relevant pH values⁴² of 5, 6, 6.8, and 8 in DI water, at a reference Pb^{2+} concentration of 15 ppb (EPA limit)⁸.

A testing protocol identical to the above (Fig. 1e, Fig. 5) is implemented, where DI water (pH = 6.8) is used to obtain the sensor reference wavelength (λ_0) and subsequent shift ($\lambda_s - \lambda_0$) after analyte flush. Similarly, the sensor inferred concentration is determined from Fig. 5b. Figure 7b shows the measured sensor spectra before (λ_0) and after analyte flush (λ_s) at analyte pH values of 5, 6, 6.8, and 8, indicating a ($\lambda_s - \lambda_0$)/sensor inferred concentration (Fig. 5b) of 0.278 nm/8.4 ppb, 0.512 nm/15.3 ppb, 0.504 nm/15 ppb and 0.502 nm/15 ppb respectively. In order to further validate the photonic sensor accuracy with changing pH, six separate sensors ($n = 6$) are measured at each pH value, where $\text{Conc.}_{\text{mean}}$, $\sigma_{\text{conc.}}$, and Err. are indicated in Table 2. As a comparison to Fig. 5, where the pH of the analyte is 6.8, similar levels of detection accuracies are observed at pH of 6–8. However, a noticeable drop in detection accuracy can be seen when the pH is lower than 6 defining the lower pH operating range of the sensor. This is anticipated, and in-line with the XPS measurement at Fig. 7a. The pH operating range (6–8) of the photonic sensor provides coverage for common environmental conditions⁴², indicating its versatility to be applied in a multitude of situations without the need for pH control.

To evaluate the effectiveness of the photonic sensor in real-life applications, the technology was deployed to quantify field-collected samples. First of all, tap, lake, and sea water are subjected to ICP-MS for elemental analysis, where the Pb concentrations are found to be 2, 5,

Table 1 | Detection accuracy and repeatability ($\text{Conc.}_{\text{mean}}/\sigma_{\text{conc.}}/\text{Err.}$) of the crown ether decorated SiP Pb^{2+} sensor against reference Pb^{2+} concentrations, in DI water, verified by ICP-MS

| Reference Pb^{2+} concentration in analyte (DI water, pH = 6.8) | Inferred $\text{Conc.}_{\text{mean}}/\sigma_{\text{conc.}}$ ($n = 6$) / Err. |
|--|--|
| 1 ppb | 1.24 ppb/ 0.26 ppb/24.0% |
| 10 ppb | 10.2 ppb/ 0.3 ppb/2.0% |
| 15 ppb | 14.3 ppb/ 0.6 ppb/4.7% |
| 80 ppb | 79.0 ppb/ 1.7 ppb/1.3% |
| 62 ppm | 64.6 ppm/ 4.5 ppm/4.2% |

The pH of the analyte is 6.8 (see Methods). $\text{Conc.}_{\text{mean}}$ refers to mean sensor inferred concentrations. $\sigma_{\text{conc.}}$ refers to the standard deviation of the sensor-inferred concentrations. Err. refers to the variation in $\text{Conc.}_{\text{mean}}$ from the reference concentrations. Each reference Pb^{2+} concentration was measured using six independent photonic sensors ($n = 6$).

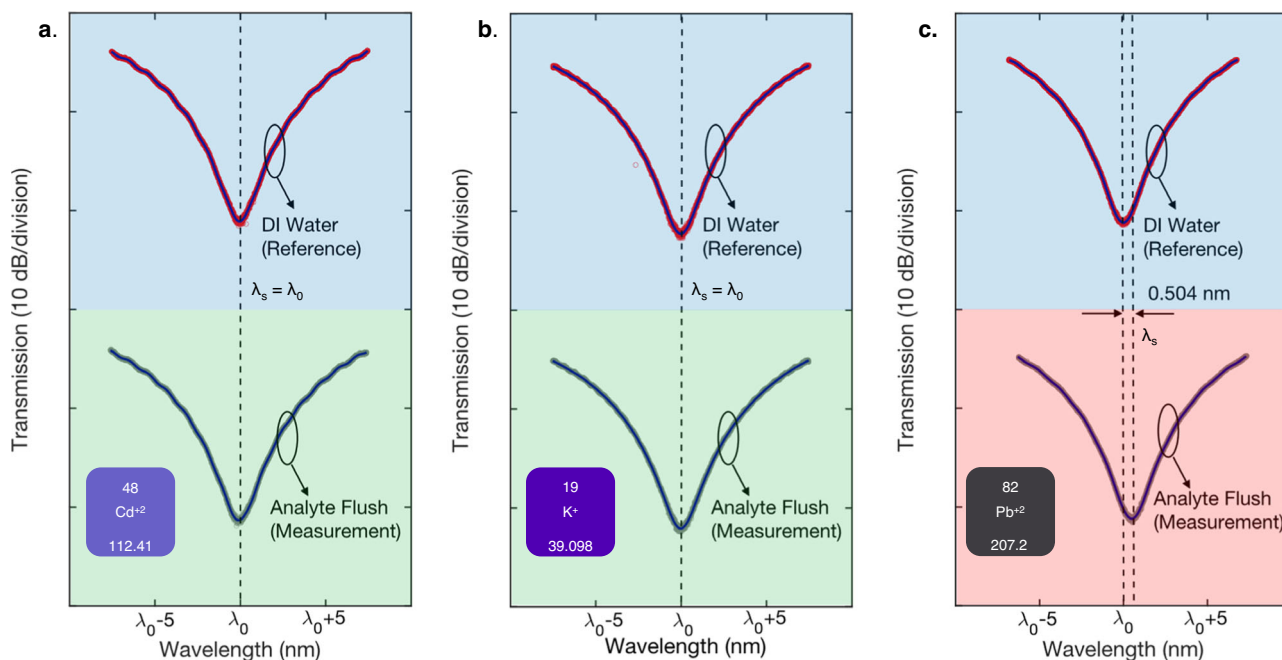


Fig. 6 | Selectivity performance of the Pb^{2+} ion photonic sensor against. a Cd^{2+} , and b, K^+ at reference concentrations of 15 ppb in DI water where no shifts in the interferometric spectra indicative of ion binding is observed. c The detection

performance of the Pb^{2+} photonic ion sensor is evaluated at reference Pb^{2+} concentrations of 15 ppb in DI water. The pH of the analyte is maintained at 6.8 (see Methods).

and 8 ppb, respectively (Supplementary Note 14). The determined pH for tap, lake, and sea water are 7.26, 7.91, and 7.79, correspondingly. Each of the environmental samples is exposed to the sensor for the measurement of Pb^{2+} concentration levels and detection accuracies in the complex matrix. An identical sensor protocol is implemented as

above with the exception of the analyte. DI water (pH = 6.8) is used to obtain the sensor reference spectrum (λ_0), and subsequent spectrum (λ_s) during analyte flush. The exposed analytes are tap, lake and sea water. Pb^{2+} concentration is inferred from the calibration curve (Fig. 5b) via $(\lambda_s - \lambda_0)$.

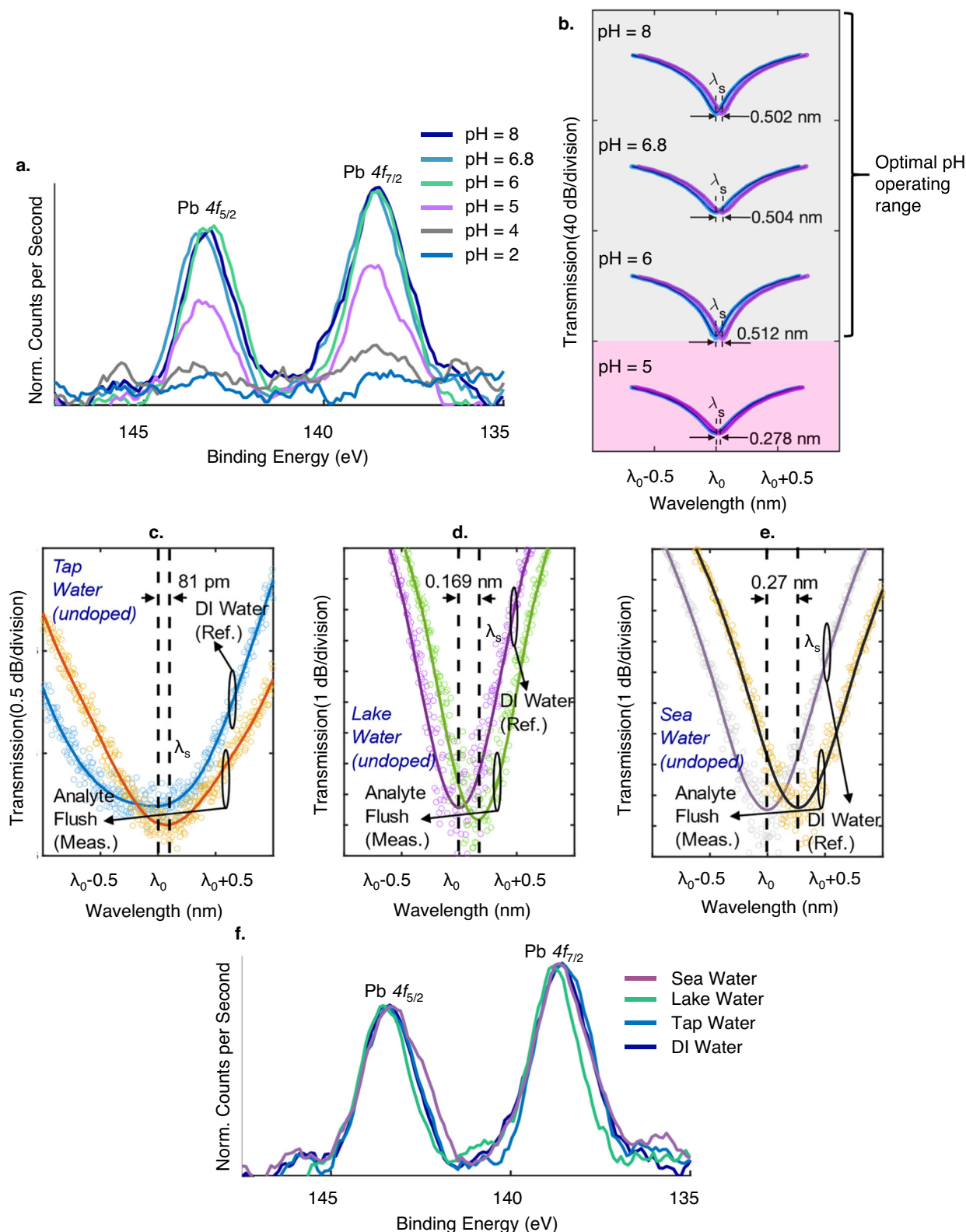


Fig. 7 | Sensor pH analysis and deployment in field samples. a Pb^{2+} XPS analysis of the crown ether functional layer across a pH range of 2–8. **b** Optical fringe minima corresponding to the detection of Pb^{2+} via the photonic sensor in **c**, tap, and **d**, lake, and **e**, sea water. **f** XPS analysis of the crown ether functional layer when the sensor is subjected to DI, tap, lake and seawater.

6, 6.8 and 8. Optical fringe minima corresponding to the detection of Pb^{2+} via the photonic sensor in **c**, tap, and **d**, lake, and **e**, sea water. **f** XPS analysis of the crown ether functional layer when the sensor is subjected to DI, tap, lake and seawater.

Figure 7c–e shows the measured ($\lambda_s - \lambda_0$) of 0.081 nm for tap water (Fig. 7c), 0.169 nm for lake water (Fig. 7d), and 0.27 nm for sea water (Fig. 7e), corresponding to sensor inferred concentrations (Fig. 5b) of 2.23, 5.06, and 8.16 ppb respectively. For further verification, the concentration of Pb^{2+} in each of these samples were synthetically increased by 15 ppb. Instances of these spectral responses are provided in Supplementary Note 15, showing ($\lambda_s - \lambda_0$)/ sensor inferred concentrations of 0.570 nm/16.9 ppb, 0.679/20.0 ppb and 0.788 nm/23.1 ppb for tap, lake and sea water respectively. To quantify the detection accuracy and repeatability of the sensor in each of the environmental samples, original and synthetically doped, repeated independent measurements ($n = 6$) are implemented using separate sensors, where the $\text{Conc.}_{\text{mean}}/\sigma_{\text{conc.}}/\text{Err.}$ are presented in Table 3. The sensor-inferred concentrations matches closely to the ground truth values. A comparison of the detection accuracy to Pb^{2+} ions in DI water (Table 1) indicates similar levels of detection accuracy as well. Further investigation into the crown ether functional layer was conducted where four separate photonic chips were exposed to Pb^{2+} in DI, tap, lake and seawater, and the $\text{Pb } 4f_{5/2}$ and $\text{Pb } 4f_{7/2}$ elemental binding energies measured via XPS. In Fig. 7f, the normalized XPS spectrum are found to be similar across all four scenarios. Accordingly, it can be concluded that the Pb^{2+} photonic sensor is resilient to elemental and organic contaminants in view of the strong affinity between the DBTDA crown ethers and Pb^{2+} ions. The pH neutrality of the environmental samples as abovementioned indicates the tendency for Pb^{2+} complexes to exist in larger proportion, in contrast to free ions. The demonstrated ability of the sensor to accurately determine Pb^{2+} concentrations levels even at complexed Pb^{2+} states imply the viability of the sensor in detecting various forms of Pb^{2+} . This is attributed to the capacity of the crown ether to displace weaker binding counterions or ligands, occupying the positions where the Pb^{2+} can form coordination bonds with the crown ether^{67,68}. This highlights one of the essential advantages of the sensor platform where sample preparation involving

multiple steps is not required; for instance, liberation of Pb^{2+} ions from its complexes using acid digestion^{69,70}.

Discussion

In this work, crown ether functionalization via Fischer esterification and subsequent amine conjugation is integrated with highly scalable inorganic SiP. This realizes an integrated chip-scale photonic sensing platform that enables the selective binding of Pb^{2+} ions, and subsequent detection down to the ppb-scale. The reaction pathway proposed and demonstrated, driven via Fischer esterification, defies prior expectations that the process is restricted to organics²⁶. This enables the engineering of the platform to selectively detect a plethora of ions via subsequent amine conjugation of various crown ethers^{27–37}. Furthermore, the functionalization process, by virtue of being solution-based, can be implemented at the wafer-scale. The reactants are dissolved in green solvents, which results in minimal environmental impact. The sensor presented in this work indicates pH resilience (6–8), with the ability to detect Pb^{2+} concentrations *in-operando*, through a wide dynamic range (1–62,000 ppb), while being highly-selective against other commonly-found, relevant ions. In addition, the viability of the sensor technology in real-life applications is demonstrated through measuring field-collected samples under environmentally relevant conditions. This work represents an encouraging step toward the ubiquitous implementation of photonic-based sensors that protects against widespread Pb^{2+} poisoning. We envisage that this platform can be extended to multiplex ion detection in multiple application spheres.

Methods

Microfluidic chamber fabrication

A custom-made acrylic top enclosure, polydimethylsiloxane (PDMS) gasket, and bottom mount make up the flow channel assembly (see Supplementary Note 3). This allows the sample solution and DI water to flow across the sensor on the photonic chips, and doubles as a containment to allow a fixed volume of sample solution to stay atop the sensor for 120 s during ion interaction. The custom-made PDMS gasket is fabricated by curing a PDMS and photo-initiator mixture (Shin-Etsu KER-4690) in polytetrafluoroethylene (PTFE) mold under a 405 nm UV lamp for 10 minutes.

Chemicals used in photonic chips functionalization

In the Fischer esterification step, polyacrylic acid ($(\text{C}_3\text{H}_4\text{O}_2)_n$) product number 323667 CAS Number: 9003-0, from Sigma-Aldrich, is coupled with the silanol group on the SiO_2 surface on the photonic chips, in the presence of tin (II) chloride (SnCl_2) catalyst, product number 323667 CAS Number: product number 208256 CAS Number: 9003-0, with a purity of 98%, from Sigma-Aldrich. The amine conjugation of the selected DBTDA crown ether, product number 294721.

Table 2 | Detection accuracy and repeatability ($\text{Conc.}_{\text{mean}}/\sigma_{\text{conc.}}/\text{Err.}$) of the crown ether decorated SiP Pb^{2+} sensor against analyte pH, using DI water, with reference Pb^{2+} concentrations of 15 ppb, verified by ICP-MS

| Analyte pH (DI water, reference Pb^{2+} concentration = 15 ppb) | Inferred $\text{Conc.}_{\text{mean}}/\sigma_{\text{conc.}}$ ($n = 6$)/ Err. |
|--|---|
| pH = 5 | 8.2 ppb/ 0.5 ppb/45.3% |
| pH = 6 | 14.7 ppb/ 0.5 ppb/2.0% |
| pH = 6.8 | 15.5 ppb/ 0.7 ppb/3.3% |
| pH = 8 | 14.8 ppb/ 0.6 ppb/1.3% |

$\text{Conc.}_{\text{mean}}$ refers to mean sensor inferred concentrations. $\sigma_{\text{conc.}}$ refers to standard deviation of the sensor-inferred concentrations. Err. refers to the variation in $\text{Conc.}_{\text{mean}}$ from the reference concentrations. Each analyte pH was measured using six independent photonic sensors ($n = 6$).

Table 3 | Detection accuracy and repeatability ($\text{Conc.}_{\text{mean}}/\sigma_{\text{conc.}}/\text{Err.}$) of the crown ether decorated SiP Pb^{2+} sensor in environmental-related scenarios (tap, lake, sea water), using the respective samples, where the Pb^{2+} concentrations are verified by ICP-MS

| Field samples | Inferred $\text{Conc.}_{\text{mean}}/\sigma_{\text{conc.}}$ ($n = 6$)/ Err. |
|---|---|
| Tap water, undoped; 2 ppb of Pb^{2+} , measured by ICP-MS | 2.40 ppb/ 0.3 ppb/20.0% |
| Lake water, undoped; 5 ppb of Pb^{2+} , measured by ICP-MS | 4.77 ppb/ 0.6 ppb/4.6% |
| Sea water, undoped; 8 ppb of Pb^{2+} ; measured by ICP-MS | 8.16 ppb/ 0.4 ppb/2.0% |
| Doped tap water, where Pb^{2+} concentration is synthetically increased by 15 ppb to 17 ppb, measured by ICP-MS | 16.7 ppb/ 0.5 ppb/1.8% |
| Doped lake water, where Pb^{2+} concentration is synthetically increased by 15 ppb to 20 ppb, measured by ICP-MS | 19.5 ppb/ 0.7 ppb/2.5% |
| Doped sea water, where Pb^{2+} concentration is synthetically increased by 15 ppb to 23 ppb, measured by ICP-MS | 22.8 ppb/ 0.7 ppb/0.9% |

$\text{Conc.}_{\text{mean}}$ refers to mean sensor inferred concentrations. $\sigma_{\text{conc.}}$ refers to the standard deviation of the sensor-inferred concentrations. Err. refers to the variation in $\text{Conc.}_{\text{mean}}$ from the reference concentrations. The measured pH of the tap, lake and sea water are 7.26, 7.91 and 7.79, respectively.

CAS Number: 69703-25-9, with a purity of 97%, from Sigma-Aldrich, with the carboxylic acid group, is carried out in the presence of 1-Ethyl-3-(3-dimethylaminopropyl)-carbodiimide (EDC) product number 03450, CAS Number: 25952-53-8, with a purity of $\geq 98\%$, from Sigma-Aldrich and N-Hydroxysuccinimide (NHS) product number 130672 CAS Number:

6066-82-6, with a purity of 98%, from Sigma-Aldrich dissolved in ethanol, product number 459844 CAS Number: 64-17-5, with a purity of $\geq 99.5\%$, from Sigma-Aldrich.

In the final rinsing step, 0.1 M nitric acid (HNO_3) used to remove as much of tin catalyst adsorbed on the surface as possible was prepared by diluting concentrated HNO_3 , product number 438073 CAS Number: 7697-37-2, with a purity of 70%, from Sigma-Aldrich.

Analyte preparation

For the measurements performed in Figs. 4–6, Supplementary Note 6 and 13, the analyte solution preparation is carried out by diluting 1000 ppm ICP standard solution of the selected ions (TraceCERT[®] from Merck) with DI water to the concentration required. For low concentrations (lower than 10 ppm), multiple rounds of dilution were performed. ICP-MS is used to verify the concentrations. The pH of the analyte is maintained at 6.8, verified through a pH meter.

To determine the selectivity of the crown ether decorated SiP sensing platform, the functional layer (Fig. 3) and the photonic sensor (Fig. 6) are tested against Na^+ , K^+ , Mg^{2+} , Li^{2+} , Zn^{2+} , Ca^{2+} , Fe^{2+} , Cu^{2+} , Al^{3+} , Sn^{2+} , Cd^{2+} and Pb^{2+} in DI water at concentrations of 100 and 15 ppb respectively. The concentrations are verified using ICP-MS. The dilution methods is elaborated above, in DI water.

To determine sensor detection accuracy as a function of pH (Fig. 7a, b), sodium hydroxide (NaOH), product number 221465 CAS Number: 1310-73-2, with a purity of $\geq 97\%$, from Sigma-Aldrich, and nitric acid (HNO_3), product number 438073 CAS Number: 7697-37-2, with a purity of 70%, from Sigma-Aldrich, are utilized in DI water to obtain analyte with pH ranging from 2 to 8 first, verified using a pH meter. Following, the dilution methods to 15 ppb of Pb^{2+} remain the same as above. The concentrations are verified using ICP-MS.

For the deployment of the sensor in environmentally related situations (Fig. 7c–f, Supplementary Note 15), water samples are collected from the tap, lake, and sea. The tap water is collected from the washroom in Nanyang Technological University, School of Electrical and Electronic Engineering, 50 Nanyang Avenue, 639798, Singapore. The lake and sea water sources are Jurong Lake Garden, 104 Yuan Ching Road, 618665, Singapore, and West Coast Park Beach, West Coast Ferry Road, 126978, Singapore, respectively. The pH of the tap, lake and sea water are 7.26, 7.91, and 7.79, respectively. ICP-MS is utilized to assess the concentration of the elemental distribution of the samples (See Supplementary Note 14). The concentration of Pb^{2+} in tap, lake and sea water are found to be 2, 5 and 8 ppb, respectively. For further testing of the environmental samples, the concentration of Pb^{2+} are synthetically increased by 15 ppb; implemented via the dilution methods mentioned above. The ground truth Pb^{2+} concentration values of the synthetically doped tap, lake and sea water are 17, 20, and 23 ppb, verified by ICP-MS.

Fundamental TE maintenance

The Pb^{2+} photonic sensor is designed for fundamental TE operation. Fundamental TE operation is crucial for the maintenance of interference fringes corresponding to the mode, as well as fringe visibility. In order to ensure that the device is operating with only the fundamental TE mode, we utilized a chain of cascaded Multi-Mode Interferometer (MMI) structures that is optimized for the desired polarization ($10 \times \text{MMI}$). The polarization-dependent loss the TM mode experience over TE is 2 dB per MMI. Cascading 10 MMIs yields a TM against TE polarization extinction ratio of 20 dB. By optimizing the

input polarization corresponding to the maximum optical power at the output, we will be able to ensure that the device operates with only the fundamental TE mode.

Measurement of the calibration curve via a cumulative approach

The following is implemented for the measurement of the calibration curve. Pb^{2+} ions are diluted in DI water. The pH of the following analyte is maintained at 6.8. DI water was first added to obtain the reference wavelength (λ_0), and then flushed from the microfluidic chamber (Step 1). Next, DI water containing Pb^{2+} was added and held for 120 s to facilitate the binding of Pb^{2+} to the functional surface at the sensing region (Step 2). The analyte was then removed again and DI water is added, where the resonant wavelength (λ_s) is measured to remove the unbound species (Step 3). The shift in wavelength is determined by ($\lambda_s - \lambda_0$). For the 6 concentrations that were measured (5, 25, 625, 2625, 62,625, 262,625 ppb), an additive approach was used. In Step 2, DI water containing 5, 20, 600, 2000, 60,000, 200,000 ppb of Pb^{2+} is added sequentially as the exposed concentration is increased. The measurement was repeated six times ($n=6$) for each set of concentrations involving each photonic sensors, as indicated by the associated error bars in Fig. 5b.

Reporting summary

Further information on research design is available in the Nature Portfolio Reporting Summary linked to this article.

Data availability

The data supporting the findings of this study are available from the article and its Supplementary Information. Due to competing interests with regards to the attempts at the commercialization of this sensor technology by Fingate Technologies Pte. Ltd. and Vulcan Photonics SDN. BHD., the source data is available from the corresponding author upon request.

References

1. Dudev, T., Grauffel, C. & Lim, C. How Pb^{2+} Binds and Modulates Properties of Ca^{2+} -Signaling Proteins. *Inorg. Chem.* **57**, 14798–14809 (2018).
2. Cory-Slechta, D. A. Legacy of Lead Exposure: Consequences for the Central Nervous System. *Otolaryngol. Head. Neck Surg.* **114**, 224–226 (1996).
3. Edwards, M. Fetal Death and Reduced Birth Rates Associated with Exposure to Lead-Contaminated Drinking Water. *Environ. Sci. Technol.* **48**, 739–746 (2014).
4. Ferreira de Mattos, G., Costa, C., Savio, F., Alonso, M. & Nicolson, G. L. Lead poisoning: acute exposure of the heart to lead ions promotes changes in cardiac function and $\text{Ca}_v1.2$ ion channels. *Biophys. Rev.* **9**, 807–825 (2017).
5. Samarghandian, S. et al. A systematic review of clinical and laboratory findings of lead poisoning: lessons from case reports. *Toxicol. Appl. Pharmacol.* **429**, 115681 (2021).
6. Rothschild, E. O. Lead Poisoning — The Silent Epidemic. *N. Engl. J. Med.* **283**, 704–705 (1970).
7. THE WHITE HOUSE. FACT SHEET: The Biden-Harris Lead Pipe and Paint Action Plan. <https://www.whitehouse.gov/briefing-room/statements-releases/2021/12/16/fact-sheet-the-biden-harris-lead-pipe-and-paint-action-plan/> (2021).
8. Understanding the Lead and Copper Rule. <https://www.epa.gov/dwreginfo/lead-and-copper-rule#:~:text=The%20rule%20replaced%20the%20previous,copper%20within%20the%20distribution%20system> (2023).
9. Gottesfeld P. The Environmental And Health Impacts Of Lead Battery Recycling. https://wedocs.unep.org/bitstream/handle/20.500.11822/13943/1_ECOWAS%20lead%20background%202016.pdf (2016).

- Almost 1 million people die every year due to lead poisoning, with more children suffering long-term health effects. <https://www.who.int/news/item/23-10-2022-almost-1-million-people-die-every-year-due-to-lead-poisoning-with-more-children-suffering-long-term-health-effects> (2022).
- Yap, S. H. K. et al. An Advanced Hand-Held Microfiber-Based Sensor for Ultrasensitive Lead Ion Detection. *ACS Sens* **3**, 2506–2512 (2018).
- Kriss, R., Pieper, K. J., Parks, J. & Edwards, M. A. Challenges of Detecting Lead in Drinking Water Using at-Home Test Kits. *Environ. Sci. Technol.* **55**, 1964–1972 (2021).
- Munir, A. et al. Selective and simultaneous detection of Zn²⁺, Cd²⁺, Pb²⁺, Cu²⁺, Hg²⁺ and Sr²⁺ using surfactant modified electrochemical sensors. *Electrochim. Acta* **323**, 134592 (2019).
- Zhang, T. et al. Detection of trace Cd²⁺, Pb²⁺ and Cu²⁺ ions via porous activated carbon supported palladium nanoparticles modified electrodes using SWASV. *Mater. Chem. Phys.* **225**, 433–442 (2019).
- Du, X. et al. A Fluorescence Sensor for Pb²⁺ Detection Based on Liquid Crystals and Aggregation-Induced Emission Luminogens. *ACS Appl. Mater. Interfaces* **13**, 22361–22367 (2021).
- Liu, J. & Lu, Y. Accelerated Color Change of Gold Nanoparticles Assembled by DNAzymes for Simple and Fast Colorimetric Pb²⁺ Detection. *J. Am. Chem. Soc.* **126**, 12298–12305 (2004).
- Kita, D. M. et al. High-performance and scalable on-chip digital Fourier transform spectroscopy. *Nat. Commun.* **9**, 4405 (2018).
- Guo, J. et al. Crown ethers in graphene. *Nat. Commun.* **5**, 5389 (2014).
- Pedersen, C. J. The Discovery of Crown Ethers (Noble Lecture). *Angew. Chem. Int. Ed. Engl.* **27**, 1021–1027 (1988).
- Pedersen, C. J. Cyclic polyethers and their complexes with metal salts. *J. Am. Chem. Soc.* **89**, 7017–7036 (1967).
- Pedersen, C. J. The Discovery of Crown Ethers. *Science (1979)* **241**, 536–540 (1988).
- Zhang, H. X. et al. Crown ether functionalized graphene oxide as ultrasensitive electrochemical sensor for detection of potassium ions. *Mater. Res. Express* **6**, 125095 (2019).
- Móczár, I. & Huszthy, P. Optically active crown ether-based fluorescent sensor molecules: A mini-review. *Chirality* **31**, 97–109 (2019).
- Zhu, M., Lerum, M. Z. & Chen, W. How To Prepare Reproducible, Homogeneous, and Hydrolytically Stable Aminosilane-Derived Layers on Silica. *Langmuir* **28**, 416–423 (2012).
- Howarter, J. A. & Youngblood, J. P. Optimization of Silica Silanization by 3-Aminopropyltriethoxysilane. *Langmuir* **22**, 11142–11147 (2006).
- Khan, Z. et al. Current developments in esterification reaction: A review on process and parameters. *J. Ind. Eng. Chem.* **103**, 80–101 (2021).
- Esteban, D. et al. Cadmium(II) and Lead(II) Complexes with Novel Macrocyclic Receptors Derived from 1,10-Diaza-15-crown-5. *Eur. J. Inorg. Chem.* **2000**, 1445–1456 (2000).
- Wang, D.-M. et al. Polymer Gels Containing Dibenzo-24-Crown-8 Ether Moieties for Removal of Cesium Ions from Aqueous Environment. *Trans. Mater. Res. Soc. Jpn.* **44**, 217–220 (2019).
- Cooper, T. E., Carl, D. R., Oomens, J., Steill, J. D. & Armentrout, P. B. Infrared Spectroscopy of Divalent Zinc and Cadmium Crown Ether Systems. *J. Phys. Chem. A* **115**, 5408–5422 (2011).
- Kumbhat, S. & Singh, U. A potassium-selective electrochemical sensor based on crown-ether functionalized self assembled monolayer. *J. Electroanal. Chem.* **809**, 31–35 (2018).
- Ganjali, M. R., Moghimi, A. & Shamsipur, M. Beryllium-Selective Membrane Electrode Based on Benzo-9-crown-3. *Anal. Chem.* **70**, 5259–5263 (1998).
- Gupta, V. K., Jain, A. K. & Kumar, P. PVC-based membranes of N,N'-dibenzyl-1,4,10,13-tetraoxa-7,16-diazacyclooctadecane as Pb(II)-selective sensor. *Sens. Actuators B Chem.* **120**, 259–265 (2006).
- Abou, D. S. et al. Towards the stable chelation of radium for biomedical applications with an 18-membered macrocyclic ligand. *Chem. Sci.* **12**, 3733–3742 (2021).
- Oral, I. & Abetz, V. Improved alkali metal ion capturing utilizing crown ether-based diblock copolymers in a sandwich-type complexation. *Soft Matter* **18**, 934–937 (2022).
- Kazemi, S. Y. & Hamidi, A. S. Competitive Removal of Lead(II), Copper(II), and Cadmium(II) Ions through a Bulk Liquid Membrane Containing Macrocyclic Crown Ethers and Oleic Acid as Ion Carriers. *J. Chem. Eng. Data* **56**, 222–229 (2011).
- Gatto, V. J. & Gokel, G. W. Syntheses of calcium-selective, substituted diaza-crown ethers: a novel, one-step formation of bibracchialariat ethers (BiBLES). *J. Am. Chem. Soc.* **106**, 8240–8244 (1984).
- Vaidya, B., Porter, M. D., Utterback, M. D. & Bartsch, R. A. Selective Determination of Cadmium in Water Using a Chromogenic Crown Ether in a Mixed Micellar Solution. *Anal. Chem.* **69**, 2688–2693 (1997).
- Sia, J. X. B. et al. Wafer-Scale Demonstration of Low-Loss (~0.43 dB/cm), High-Bandwidth (>38 GHz), Silicon Photonics Platform Operating at the C-Band. *IEEE Photonics J.* **14**, 1–9 (2022).
- Demir, F. & Derun, E. M. Modelling and optimization of gold mine tailings based geopolymer by using response surface method and its application in Pb²⁺ removal. *J. Clean. Prod.* **237**, 117766 (2019).
- Barakat, M. A., Ramadan, M. H., Kuhn, J. N. & Woodcock, H. L. Equilibrium and kinetics of Pb²⁺ adsorption from aqueous solution by dendrimer/titania composites. *Desalinat. Water Treat.* **52**, 5869–5875 (2014).
- Chowdhury, I. R., Chowdhury, S., Mazumder, M. A. J. & Al-Ahmed, A. Removal of lead ions (Pb²⁺) from water and wastewater: a review on the low-cost adsorbents. *Appl. Water Sci.* **12**, 185 (2022).
- Jurgens, B. C., Parkhurst, D. L. & Belitz, K. Assessing the Lead Solubility Potential of Untreated Groundwater of the United States. *Environ. Sci. Technol.* **53**, 3095–3103 (2019).
- Kita, D. M., Michon, J., Johnson, S. G. & Hu, J. Are slot and sub-wavelength grating waveguides better than strip waveguides for sensing? *Optica* **5**, 1046–1054 (2018).
- Luan, E., Shoman, H., Ratner, D. M., Cheung, K. C. & Chrostowski, L. Silicon Photonic Biosensors Using Label-Free Detection. *Sensors* **18**, 3519 (2018).
- Sia, J. X. B. et al. Mid-Infrared, Ultra-Broadband, Low-Loss, Compact Arbitrary Power Splitter Based on Adiabatic Mode Evolution. *IEEE Photonics J.* **11**, 1–11 (2019).
- Palmer, R. et al. Low-Loss Silicon Strip-to-Slot Mode Converters. *IEEE Photonics J.* **5**, 2200409 (2013).
- Puumala, L. S. et al. An Optimization Framework for Silicon Photonic Evanescent-Field Biosensors Using Sub-Wavelength Gratings. *Biosens. (Basel)* **12**, 840 (2022).
- Liu, Q. et al. Highly sensitive Mach-Zehnder interferometer biosensor based on silicon nitride slot waveguide. *Sens. Actuators B Chem.* **188**, 681–688 (2013).
- Wang, L. et al. Complexation mechanism of crown ethers with rubidium and cesium ions using density functional theory. *Comput. Theor. Chem.* **1225**, 114139 (2023).
- Wang, Q., Wang, X. & Li, L. Density functional theory study on a fluorescent chemosensor device of aza-crown ether. *J. Phys. Org. Chem.* **27**, 546–554 (2014).
- Vetri, P. et al. A DFT study on structural and bonding analysis of transition-metal carbonyls [M(CO)₄] with terminal silicon chalcogenides complexes [M(CO)₃SiX] (M = Ni, Pd, and Pt; X = O, S, Se, and Te). *Comput. Theor. Chem.* **1226**, 114214 (2023).
- Salmahaminati, Abe, M., Purnama, I., Mulyana, J. Y. & Hada, M. Density Functional Study of Metal-to-Ligand Charge Transfer and Hole-Hopping in Ruthenium(II) Complexes with Alkyl-Substituted Bipyridine Ligands. *ACS Omega* **6**, 55–64 (2021).

53. Casas, A., Ramos, M. J., Rodríguez, J. F. & Pérez, Á. Tin compounds as Lewis acid catalysts for esterification and transesterification of acid vegetable oils. *Fuel Process. Technol.* **106**, 321–325 (2013).
54. Fischer, M. J. E. Amine Coupling Through EDC/NHS: A Practical Approach. in *Surface Plasmon Resonance: Methods and Protocols* (ed. Mol Nico J. and Fischer, M. J. E.) vol. 627, 55–73 (Humana Press, Totowa, NJ, 2010). https://doi.org/10.1007/978-1-60761-670-2_3.
55. Hüfner S. *Photoelectron Spectroscopy Principles and Applications*. vol. 82, 636–641 (Springer-Verlag Berlin Heidelberg New York, Berlin Heidelberg New York, 2003).
56. Aris, A. Z., Kam, R. C. Y., Lim, A. P. & Praveena, S. M. Concentration of ions in selected bottled water samples sold in Malaysia. *Appl. Water Sci.* **3**, 67–75 (2013).
57. Vu, H., Merkel, B. & Wiche, O. Major ions, trace elements and evidence of groundwater contamination in Hanoi, Vietnam. *Environ. Earth Sci.* **81**, 305 (2022).
58. Abd Elnabi, M. K. et al. Toxicity of Heavy Metals and Recent Advances in Their Removal: A Review. *Toxics* **11**, 580 (2023).
59. Liu, Y., Lotero, E. & Goodwin, J. G. Effect of water on sulfuric acid catalyzed esterification. *J. Mol. Catal. A Chem.* **245**, 132–140 (2006).
60. da Silva, M. J., Julio, A. A. & dos Santos, K. T. Sn(II)-catalyzed β -citronellol esterification: a Brønsted acid-free process for synthesis of fragrances at room temperature. *Catal. Sci. Technol.* **5**, 1261–1266 (2015).
61. Xie, W., Wang, H. & Li, H. Silica-Supported Tin Oxides as Heterogeneous Acid Catalysts for Transesterification of Soybean Oil with Methanol. *Ind. Eng. Chem. Res.* **51**, 225–231 (2012).
62. Baek, H., Minakawa, M., Yamada, Y. M. A., Han, J. W. & Uozumi, Y. In-Water and Neat Batch and Continuous-Flow Direct Esterification and Transesterification by a Porous Polymeric Acid Catalyst. *Sci. Rep.* **6**, 25925 (2016).
63. Buttersack, C. Modeling of type IV and V sigmoidal adsorption isotherms. *Phys. Chem. Chem. Phys.* **21**, 5614–5626 (2019).
64. Altun, A. O., Bond, T., Pronk, W. & Park, H. G. Sensitive Detection of Competitive Molecular Adsorption by Surface-Enhanced Raman Spectroscopy. *Langmuir* **33**, 6999–7006 (2017).
65. Golcs, Á., Vezse, P., Ádám, B. Á., Huszthy, P. & Tóth, T. Comparison in practical applications of crown ether sensor molecules containing an acridone or an acridine unit – a study on protonation and complex formation. *J. Incl. Phenom. Macrocycl. Chem.* **101**, 63–75 (2021).
66. Lundgren, R. J. & Stradiotto, M. Key Concepts in Ligand Design. in *Ligand Design in Metal Chemistry* 1–14 (John Wiley & Sons, Ltd, 2016). <https://doi.org/10.1002/9781118839621.ch1>.
67. Kawai, Y., Fujinaga, S., Hashimoto, M. & Tsukagoshi, K. Separation of Metal Complexes with Counter Ions by Tube Radial Distribution Chromatography Using a Ternary Solvent Containing 8-quinolinol. *Anal. Sci.* **31**, 1177–1182 (2015).
68. Teichert, J. & Ruck, M. Influence of Common Anions on the Coordination of Metal Cations in Polyalcohols. *Eur. J. Inorg. Chem.* **2019**, 2267–2276 (2019).
69. Douvris, C., Vaughan, T., Bussan, D., Bartzas, G. & Thomas, R. How ICP-OES changed the face of trace element analysis: Review of the global application landscape. *Sci. Total Environ.* **905**, 167242 (2023).
70. Wilschefska, S. C. & Baxter, R. M. Inductively Coupled Plasma Mass Spectroscopy: Introduction to Analytical Aspects. *Clin. Biochem. Rev.* **40**, 115–133 (2019).
- was performed in part through the use of the facilities of MIT.nano, Harvard University Center for Nanoscale Systems (CNS), NTU's Centre for Micro- & Nano-Electronics (CMNE) and Nanyang Nanofabrication Centre (N2FC). The authors also wish to acknowledge this collaborative work with Fingate Technologies and Vulcan Photonics.

Author contributions

J.X.B.S., L.R., Y.Z.T. conceived the idea to integrate crown ethers with silicon photonics for ion detection with the help from C.S.O., X.G., K.N.K., X.L., W.W., S.S., C.L., R.R., C.G.L., G.T.R., J.J.H., H.W., Y.Z.T. conceived the functionalization process flow. L.R. did the photonic design and fabrication. X. G. did the photonic sensor characterization. K.N.K. did the material characterization with the help from Y.Z.T. and C.S.O. Y.Z.T. and G.X. designed and constructed the sensor assembly. L.R., Y.Z.T., J.J.H. and J.X.B.S. wrote the manuscript with inputs from C.S.O., X.G., K.N.K., X.L., W.W., S.S., C.L., R.R., C.G.L., G.T.R., H. J.X. B.S., H.W. and J.J.H. supervised the project.

Competing interests

Y. Z. T., C. S. O. and K. N. K. have filed patent applications on the chemical synthesis methods and sensor design described in the manuscript; PCT/MY2022/050092, PCT/MY2022/050093, PCT/MY2022/050095, PCT/MY2022/050096, PCT/MY2022/050125, PCT/MY2022/050132, PCT/MY2022/050134, PCT/MY2023/050020. Fingate Technologies Pte Ltd and Vulcan Photonics SDN. BHD. are working on the commercialization of the photonic sensor technology described in the manuscript. The remaining authors declare no competing interests.

Additional information

Supplementary information The online version contains supplementary material available at <https://doi.org/10.1038/s41467-024-47938-6>.

Correspondence and requests for materials should be addressed to Jia Xu Brian Sia.

Peer review information *Nature Communications* thanks Hong Chen, and Woo Hyoung Lee for their contribution to the peer review of this work. A peer review file is available.

Reprints and permissions information is available at <http://www.nature.com/reprints>

Publisher's note Springer Nature remains neutral with regard to jurisdictional claims in published maps and institutional affiliations.

Open Access This article is licensed under a Creative Commons Attribution 4.0 International License, which permits use, sharing, adaptation, distribution and reproduction in any medium or format, as long as you give appropriate credit to the original author(s) and the source, provide a link to the Creative Commons licence, and indicate if changes were made. The images or other third party material in this article are included in the article's Creative Commons licence, unless indicated otherwise in a credit line to the material. If material is not included in the article's Creative Commons licence and your intended use is not permitted by statutory regulation or exceeds the permitted use, you will need to obtain permission directly from the copyright holder. To view a copy of this licence, visit <http://creativecommons.org/licenses/by/4.0/>.

© The Author(s) 2024

Acknowledgements

Jia Xu Brian Sia would like to acknowledge Ministry of Education/NTU College of Engineering International Postdoctoral Fellowship. This work